AIAA JOURNAL
Vol. 60, No. 10, October 2022

Determining Flow Propagation Direction from In-Flight Array Surface Pressure Fluctuation Data

Stefan Haxter,* Hans-Georg Raumer,† Tobias Berkefeld,‡ and Carsten Spehr§
DLR, German Aerospace Center, 37073 Göttingen, Germany

https://doi.org/10.2514/1.J061711

When characterizing spatial coherence properties of turbulent boundary-layer surface pressure fluctuation data, it is important to determine the local flow direction first. Without flow direction, it is very easy to introduce errors due to misalignment between sensors and the flow. For cases with two-dimensional microphone distributions, a method of determining flow direction from the orientation of the coherent pressure in spatial domain was introduced recently. If the data are analyzed in wavenumber domain, flow information can be obtained by the position and orientation of the convective ridge. In this publication, flow directions determined from a revised spatial domain approach and from two wavenumber domain approaches are considered. It was found that the result from the spatial domain approach and the result from the orientation of the convective ridge are similar for most frequencies, while the result based on the position of the convective ridge differs in the lower frequency range. Tilted convection of coherent structures in the turbulent boundary layer is discussed as a possible cause of these observations. A modification of the analytical model for surface pressure coherence is derived that takes the findings into account.

Downloaded by DLR DEUTSCHES ZENTRUM FUER LUFT UND RAUMFAHRT on December 13, 2022 | http://arc.aiaa.org | DOI: 10.2514/1.J061711

Nomenclature

b	=	wavenumber dirty map
e	=	steering vector
f	=	frequency
H	=	Hermitian transpose
i	=	imaginary unit
$\mathcal{K}$	=	steering grid in wavenumber domain
k^{center}	=	center of convective ridge
k_c	=	convective wavenumber based on convective velocity
k_x, k_y	=	wavenumber
k_φ	=	convective wavenumber based on phase velocity
L	=	window size
l_x, l_y	=	coherence lengths
$\mathbb{M}$	=	arithmetic mean
M	=	number of signal averages
N	=	number of transducers
R	=	cross-spectral matrix
$s, \hat{s}$	=	slope
$\top$	=	transpose
u_c	=	convective velocity
u_φ	=	phase velocity
w	=	weighting function
x, y	=	transducer position
x', y'	=	transducer position in flow coordinates
α	=	tilt angle of convective ridge
$\hat{\alpha}$	=	tilt angle of coherence pattern
β	=	angle to center of the convective ridge
γ	=	coherence
λ	=	wavelength
ξ, η	=	transducer separation
ξ', η'	=	rotated transducer separation
ϕ	=	spectrum
ω	=	angular frequency

Subscripts

k	=	averaging window index
n, m	=	transducer indices
x	=	length direction
y	=	cross direction

I. Introduction

KNOWLEDGE of the characteristics of pressure fluctuations is important for predicting the aerovibro acoustic excitation of surface panels exposed to a boundary-layer flow. One of these characteristic features is the direction in which the flow is propagating locally on the surface. There are two reasons for the importance: firstly, an erroneous assumption on flow direction may introduce an error when trying to determine the coherence length in the direction of flow [1]; secondly, a similar error can be introduced when predicting structural vibration by matching the convective ridge of the turbulent boundary-layer pressure fluctuations with the modal acceptance of the underlying structure. An error in the position of the convective ridge can lead to the wrong structural modes to be excited in the prediction. It will be shown that the position and orientation of the convective ridge in the wavenumber domain in part differ greatly from expected values. This was found when three methods for determining the local flow angle from the surface pressure fluctuations were compared. The shift in position is traced back to an oblique/tilted convection of coherent structures in the turbulent boundary layer as sketched in Fig. 1.

For most scenarios in experimental aeroacoustics, determining the local flow direction is not the predominant question to be answered. In wind tunnel measurements for instance, the main flow direction is known as it is aligned with the test section orientation. Experimental [2–4] and numerical [5] investigations have therefore focused on the magnitude of the determined flow velocity rather than its direction. Reasonably, the sensor arrays were implicitly assumed to align with the flow. In flight testing some effort has to be taken in order to determine the local flow direction as the flowfield is in part influenced by large pressure gradients. Regions on the fuselage where adverse and favorable pressure gradients are to be expected were sketched out by Gyorgyfalvy [6].

Panton et al. [7] performed flight tests on a Schweizer 2-32 sailplane for determining characteristics of pressure fluctuations during flight. Before the flight test, a study was conducted to find both a region of constant pressure on the sailplane fuselage as well as the local flow direction. The latter was found by a tuft study conducted at

Presented as Paper 2017-3205 at the 23rd AIAA/CEAS Aeroacoustics Conference, Denver, CO, June 5–9, 2017; received 7 February 2022; revision received 10 June 2022; accepted for publication 12 June 2022; published online 8 July 2022. Copyright © 2022 by The Authors. Published by the American Institute of Aeronautics and Astronautics, Inc., with permission. All requests for copying and permission to reprint should be submitted to CCC at www.copyright.com; employ the eISSN 1533-385X to initiate your request. See also AIAA Rights and Permissions www.aiaa.org/randp.

*Research Scientist, Former Member of Department of Experimental Methods.

†Research Scientist, Department of Experimental Methods; hans-georg.raumer@dlr.de (Corresponding Author).

‡Research Scientist, Former Member of Department of Fluid Systems.

§Research Scientist, Department of Experimental Methods.

Downloaded by DLR DEUTSCHES ZENTRUM FUER LUFT UND RAUMFAHRT on December 13, 2022 | http://arc.aiaa.org | DOI: 10.2514/1.J061711

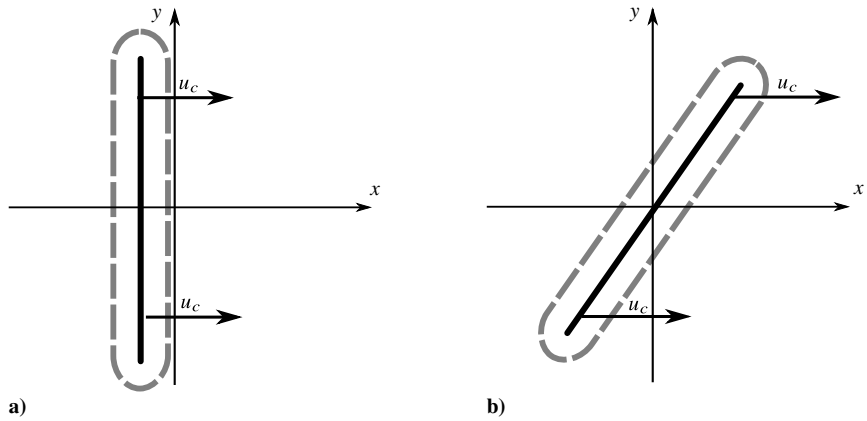

Fig. 1 Schematic diagram of regular convection of a coherent structure (a) vs tilted convection (b).

different speeds, taking external pictures of the airplane in flight to see whether some tufts attached to the fuselage would align with an array.

Similarly, Rizzi et al. [8] used an agile cone mounted on the outside of the airplane to indicate the local flow direction, which was then recorded by a video camera from the inside of the cabin for further analysis. Palumbo [9] used a similar technique where the pitch of the aircraft was varied in flight so that the flow direction—indicated by a string attached to the outside of a window—would align with a line imprinted on the window. The angle at which this line was imprinted matched the angle of a transducer array in an adjacent window of the airplane. Thus, the flow angle was roughly aligned with the transducer array. Haxter and Spehr [1] used the signal coherence plotted over the transducer spacing from an in-flight array to determine the average flow direction.

Surface pressure fluctuations are commonly evaluated either in the spatial domain (Palumbo [9] and Haxter [1]) or in the wavenumber domain (Abraham [10], Haxter [11], Bull [12], and Panda [13]). Conclusions about the flow angle can be drawn from either of the two representations.

In the spatial domain the orientation of a "coherent patch"—the cluster of transducer separations with relatively large coherence values—contains information about the flow direction [1]. The dimensions of this coherent patch resemble the characteristic lengths of surface pressure coherence or "coherence length," which has been measured frequently [9,14–17] and is used to predict both signal attenuation [18] and structural vibration [19].

In the wavenumber domain the turbulent boundary-layer pressure fluctuations are represented by the "convective ridge." Both its inclination and its center position can yield information about the flow direction.

The three methods for obtaining information about the flow direction—orientation of the coherent patch in the spatial domain as well as convective ridge orientation and center position in the wavenumber domain—are applied to the same flight test dataset and the results are compared. Not only will this yield information about the potential for structural excitation, but also this will give a comparison between the results from the three methods.

It is foreclosed that differences between the results from the three methods will occur. These differences will be used to hypothesize a skewed convection of turbulent structures in the boundary layer over the array as shown in Fig. 1. It will be differentiated between the terms "phase velocity" and "convective velocity" in order to accommodate for the differences found.

II. Experiment

The considered experimental data were measured on the Advanced Technology Research Aircraft "ATRA" (Fig. 2) flight test carrier of the Deutsches Zentrum für Luft- und Raumfahrt (DLR/German Aerospace Center) during a flight test campaign conducted in 2011/2012. The aim of this measurement campaign was to gain further insight into the transfer paths of vibrational energy into the

Fig. 2 Test carrier D-ATRA (Advanced Technology Research Aircraft). Source: DLR CC-BY 3.0.

cabin [20]. More than 350 accelerometers, microphones, and pressure transducers were placed in the section of the aircraft sketched in Fig. 3. Of all those transducers, 30 differential pressure transducers were installed in three dummy windows in the vicinity of the wing as an array. A sketch of the array projected onto a two-dimensional plane is shown in Fig. 4a. The maximum distance between the assumed flat sensor plane and the actual curved position was 2.5 mm. A reference pressure port on the center dummy window provided the reference pressure for all the transducers. The overall orientation of the array is aligned with the aircraft length axis.

The spatial separations between each transducer combinations are referred to as the "co-array" (see Fig. 4b) and are defined by

$$\begin{aligned} \xi_{nm} &= x_n - x_m \\ \eta_{nm} &= y_n - y_m \end{aligned} \tag{1}$$

Using three windows for the array leads to three clusters of transducers in the array. Therefore, the co-array consists of five clusters with the center cluster representing all transducer separations spanning one window, the intermediate clusters spanning two windows, and the outer clusters spanning three windows. The pressure transducers were of type Kulite XCL-093 with a full-scale pressure range of 5 PSI. The signals from the Kulites were pre-amplified and then routed to the data recording device of type Dewetron DEWE-818 data acquisition

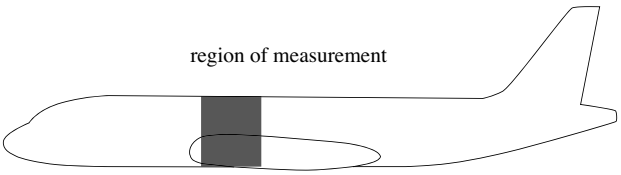

Fig. 3 Sketch of the installation region of the in-flight array in the vicinity of the wing.

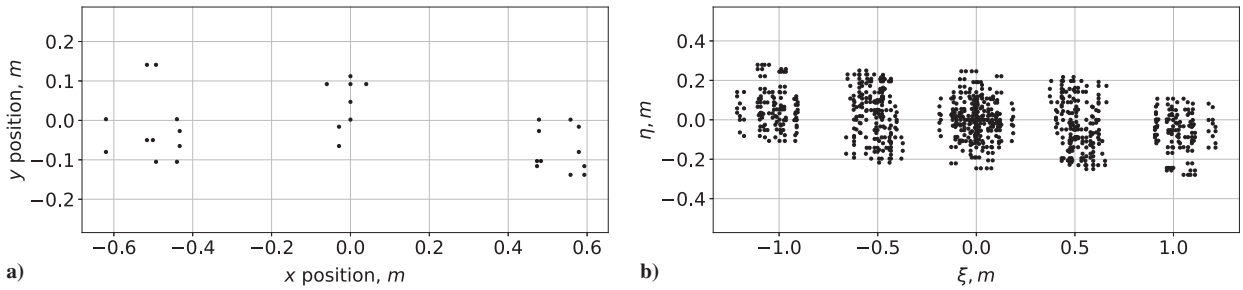

Fig. 4 a) Sketch of the array positions installed on the test carrier. The x axis coincides with the aircraft length axis. b) Sketch of the array spacings ("co-array").

Downloaded by DLR DEUTSCHES ZENTRUM FUER LUFT UND RAUMFAHRT on December 13, 2022 | http://arc.aiaa.org | DOI: 10.2514/1.J061711

system with DEWETRON DEWE-51-PCI-128 A/D-frontends. A sensor distribution was chosen in which each transducer had a neighbor element in both aircraft length and cross direction. In both directions, the spacings were chosen so that the distances would increase logarithmically when sorted. The initial assumption had been that this would provide a reasonable array under homogeneous and ergodic conditions. Because the Kulite sensors were mounted in pinholes, conducting a meaningful calibration procedure under realistic flight conditions is extremely challenging. Therefore, a calibration of the Kulite sensors was not conducted. For a deeper discussion of this aspect we refer to Sec. 3.1 of [1]. The absolute pressure of the reference pressure port was measured using a SETRA model ASM1 transducer with a pressure range of 0–16 PSI. Data were recorded at a sampling rate of 50 kHz and a bit depth of 24 bit. Electrical noise from the airborne power supply system at a frequency of 400 Hz was present on the Kulite signals. We will refer later to the disturbance by electrical noise in the Results section. The flight condition was chosen at a typical cruise flight scenario [1] (Mach number $= 0.78$), and a total time of 600 s was recorded. Further details about the flight conditions and the position of the array on the aircraft unfortunately cannot be disclosed.

At flight conditions the Helmholtz frequency of the pinholes in which the pressure transducers were mounted was estimated at 3.75 kHz. Only frequencies below will be evaluated. The reason for the sampling rate being substantially higher than the highest frequency utilizable due to Helmholtz resonator effects was that many other sensors were installed on test carrier during the campaign with all signals being recorded synchronously.

III. Signal Processing

All three data analysis methods employ the cross-spectral matrix (CSM) R of the data, which was estimated using Welch's method [21]:

$$R_{nm} = \frac{1}{M}\sum_{k=1}^{M}\left(w \cdot \phi_n^k\right) \cdot \left(w \cdot \phi_m^k\right)^H \tag{2}$$

Here w indicates the Hann weighting function, H indicates the Hermitian, and ϕ_n^k is the Fourier transform of the kth window of the signal of transducer n and of transducer m, respectively. A window size of $L = 4096$ samples was used in order to ensure both a complete propagation of turbulent structures over the entire length of the array and a large number of averages. The total number of $M = 14582$ overlapping averages was achieved using an overlap factor of $r = 0.5$. Note that the expected root mean square error introduced by the finite number of averages is of the order $C_{\mathrm{Welch}} \cdot M^{-(1/2)}$, with a constant C_{Welch}, which is close to one and depends on the window function and the overlap factor [21]. The procedure results in a matrix R for every bin center frequency of the Welch estimation, so $R \equiv R(f)$. In the following, three methods are proposed for determining the flow direction:

1) *Spatial domain approach*—For the first method, the coherence pattern of R is analyzed. This is done entirely in the spatial domain.

2) *Wavenumber domain approach: center*—For the second method, the center position of the convective ridge is analyzed. This is done in the wavenumber domain.

3) *Wavenumber domain approach: inclination*—In the third method, the inclination of the convective ridge is analyzed. This is done in the wavenumber domain as well.

A. Spatial Domain Approach

For the spatial domain approach, each element R_{nm} of the cross-spectral matrix is normalized with the diagonal elements R_{nn} and R_{mm} to obtain the square of the coherence γ^2:

$$\gamma_{nm}^2 = \frac{|R_{nm}|^2}{R_{nn} \cdot R_{mm}} \tag{3}$$

Note that the magnitude of the cross-spectral entry is taken in the numerator of Eq. (3), thus discarding any phase information contained in R_{nm}. The spatial domain approach uses a coherence model Γ given by

$$\Gamma(l_x, l_y, \hat{\alpha}, \xi, \eta) = \exp\left(-\frac{|\xi\cos\hat{\alpha} + \eta\sin\hat{\alpha}|}{l_x} - \frac{|-\xi\sin\hat{\alpha} + \eta\cos\hat{\alpha}|}{l_y}\right) \tag{4}$$

This model produces a dominant ellipsoidal pattern (coherence pattern), which is tilted by an angle $\hat{\alpha}$ (cf. Fig. 5a). Now the coherence model is fitted to the measured coherence in a least-squares sense using the coherence lengths l_x and l_y and the angle $\hat{\alpha}$ as parameters:

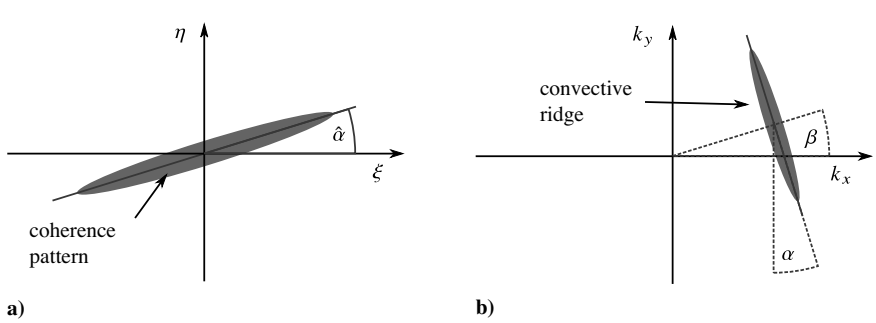

Fig. 5 a) Sketch of the coherence pattern inclination in the spatial domain. b) Sketch of a wavenumber spectrum with an inclined convective ridge.

Downloaded by DLR DEUTSCHES ZENTRUM FUER LUFT UND RAUMFAHRT on December 13, 2022 | http://arc.aiaa.org | DOI: 10.2514/1.J061711

$$l_x^\star, l_y^\star, \hat{\alpha}^\star = \underset{l_x, l_y, \hat{\alpha}}{\arg\min} \sum_{n,m=1}^{N} \left\| \gamma_{nm}^2 - \Gamma^2(l_x, l_y, \hat{\alpha}, \xi_{nm}, \eta_{nm}) \right\|_2^2 \tag{5}$$

The minimization problem (5) can be solved by a suitable nonlinear least-squares solver (e.g., the scipy curve_fit routine, which was used for this paper).

Note that the following symmetry relation holds:

$$\Gamma(l_1, l_2, \hat{\alpha}, \xi, \eta) = \Gamma\left(l_2, l_1, \hat{\alpha} + \frac{\pi}{2}, \xi, \eta\right) \tag{6}$$

This has to be taken into account for the implementation of the minimization problem (5). Note further that the method presented here differs from the method used in reference [1], where thresholding was applied to the coherence data. In this work, the entire coherence structure of the CSM is used because the former method is rather sensitive to the choice of the threshold value.

B. Wavenumber Domain Approach: Center

For the next approach a wavenumber analysis is applied on the data. The transformation is performed using a beamforming approach with planar waves (cf. [22]):

$$b(k_x, k_y, f) = \frac{e(k_x, k_y)^H R(f) e(k_x, k_y)}{N^2} \tag{7}$$

Here the steering vector e is given by a planar wave propagation model:

$$e(k_x, k_y) = \exp\Big(-2\pi i \cdot (k_x x + k_y y)\Big) \tag{8}$$

where x and y are vectors containing all instances of x_n and y_n and $i = \sqrt{-1}$. The resulting beamforming map b is a wavenumber representation of the surface pressure fluctuations over the array. The wavenumber positions k_x and k_y are chosen from a steering grid $\mathcal{K}$ to fit the desired range of wavenumbers to evaluate. The beamform map b is yet contaminated with array properties impressed on the result: the resulting map is convolved with the array's point spread function p, i.e.,

$$b = p * \Phi \tag{9}$$

A deconvolution procedure is required to remove the array's inherent point spread function p from b in order to obtain the desired underlying source map Φ. For this work this was carried out by the DAMAS2.1 [23] algorithm. Basic characteristics such as the shape of the convective ridge are, however, already visible in the "dirty" map b although they are usually strongly blurred and perturbed by noise effects. As these characteristics apply to both the one-dimensional and the two-dimensional cases, the short overview of the characteristics by Bull [12] summarizes both cases well. In boundary-layer flows, the convective ridge is a very dominant feature of the wavenumber spectrum [22,24]. It appears as a shape elongated in cross-stream direction with an offset in inflow direction (see Fig. 5b). Its center position will be denoted by k^{center}. For subsonic flows, $\|k^{\text{center}}\|_2 > k_0$ applies, where k_0 is the acoustic wavenumber. For the analysis, the convective ridge was defined as follows. Firstly, the source map Φ was divided by its global maximum to have maximum value 1 (the result is again denoted by Φ). Secondly, the convective ridge is defined as the largest connected component of the set

$$\Big\{(k_x, k_y)^\top \in \mathcal{K} : 10 \cdot \log_{10}(\Phi(k_x, k_y)) > -3\Big\}$$

Essentially, this is the largest connected region of a contour plot of the source map with a contour level of 3 dB below the global peak. The center of the convective ridge is determined by using the arithmetic mean $\mathbb{M}$ of the set of points $(k_{x,j}, k_{y,j})^\top$ attributed to the convective ridge as this has proven to be a robust approach:

$$k^{\text{center}} = \mathbb{M}\Big\{(k_{x,j}, k_{y,j})^\top\Big\} \tag{10}$$

Alternatively one may determine the center by taking, e.g., the location of the maximum of the DAMAS2.1 solution or by taking a weighted mean. The location of the center of the convective ridge results from the propagation of pressure fluctuations over the array leaving phase differences between the signals at different transducers. The velocity u_φ resulting from k^{center}

$$u_\varphi = \frac{2\pi f}{\|k^{\text{center}}\|_2} \tag{11}$$

will therefore be called *phase velocity* in the following. The propagation direction angle β of the phase of pressure fluctuations on the surface is obtained by

$$\beta = \arctan\left(\frac{k_x^{\text{center}}}{k_y^{\text{center}}}\right) \tag{12}$$

C. Wavenumber Domain Approach: Inclination

The third approach utilizes the inclination of the convective ridge in the wavenumber domain. This is shown by the angle α in Fig. 5b. This inclination is determined from the wavenumber map after subsequent deconvolution (see Sec. III.B above). For the set of points $(k_{x,j}, k_{y,j})^\top$ being part of the convective ridge, one solves a linear regression problem:

$$(\hat{s}, a) = \underset{\tilde{s}, \tilde{a}}{\arg\min} \sum_j \left\| k_{y,j} - \tilde{s} \cdot k_{x,j} - \tilde{a} \right\|_2^2 \tag{13}$$

Again, the arc tangent function is used to determine the angle from the inclination $\hat{s}$, as in Sec. III.A before. For the wavenumber inclination, however, the dominant axis of the convective ridge is inclined relative to the flow direction by $\pi/2$. This value is therefore added to the angle resulting from the angle of line inclination $\hat{s}$; i.e., the angle α is obtained by

$$\alpha = \arctan(\hat{s}) + \pi/2 \tag{14}$$

The coherence pattern is associated with the flow direction of the boundary layer [1]. It is tilted by an angle $\hat{\alpha}$ relative to the array coordinate system. This angle $\hat{\alpha}$ will also be directly connected to the inclination of the convective ridge in the wavenumber domain, α, due to the rotation property of the two-dimensional Fourier transform (cf. [25] p. 168). More precisely, if a function is rotated in spatial domain, its Fourier transform will also be rotated in the same way. The direction retrieved from the spatial coherence pattern and the inclination of the convective ridge therefore describes the direction of what will be called *convective velocity* (denoted by u_c) in the following.

D. Error Estimation

The estimation results of all three presented methods are affected by measurement errors, i.e., noisy transducer data. To quantify the resulting uncertainty for the flow angle determination, an error estimation on simulated noisy data was carried out. The exact procedure of this Monte Carlo approach and the results of the error estimation can be found in Appendix B.

IV. Results

In the following, results on the experimental dataset will be shown for the three methods introduced above: flow direction determination in the spatial domain, angle to the convective ridge center in the wavenumber domain, and convective ridge inclination in the wavenumber domain. Two exemplary bin frequencies will be chosen at

Downloaded by DLR DEUTSCHES ZENTRUM FUER LUFT UND RAUMFAHRT on December 13, 2022 | http://arc.aiaa.org | DOI: 10.2514/1.J061711

which to perform all three evaluation methods. At the higher one of the two frequencies all three analysis methods will yield similar results, while at the lower frequency the result from one of the methods differs. The choice of frequency was made to provide a good example of the difference.

A. Angle Estimation

1. *Spatial Domain*

In Fig. 6, the coherence levels γ^2 of all transducer pairs are displayed for frequencies of 769 and 2490 Hz, respectively. To highlight the coherence patches, the size of each plotted point is scaled according to its coherence level. At 769 Hz (Fig. 6a), more transducer pairs have a large value than at 2490 Hz (Fig. 6b). The larger the coherence value of a specific pair, the larger is its impact on the minimization problem in Eq. (5). The dominant coherence pattern orientation can be determined from the data and is shown as a dashed line in both figures. It is inclined relative to the x axis by 13.2° at 769 Hz and by approximately 13.6° at 2490 Hz. Such a deviation of the flow relative to the aircraft length axis has already been observed in previous flight tests (cf. [9]). We refer to Haxter [1] for a more detailed representation. Note also that the difference between those two angles is of the order of magnitude of the standard error (approximately 0.1°) that was predicted from the Monte Carlo simulation in Appendix B for the spatial method.

2. *Wavenumber Domain*

The two wavenumber domain analysis methods will be shown in parallel in the passage below. A wavenumber analysis with subsequent application of deconvolution using 10^4 iterations was performed on an equidistant wavenumber grid with 512×512 wavenumber focus points and

$$\frac{k_x}{k_0}, \quad \frac{k_y}{k_0} \in [-7, 7]$$

The characteristics of the convective ridge were evaluated using the two wavenumber domain methods. The results for the same two frequencies as in the previous section are shown in Fig. 7. Both spectra exhibit a convective ridge at positive wavenumber in the region of $k_x/k_0 \approx 1.5$. The convective ridge at 2490 Hz in Fig. 7b shows expected behavior. Its inclination angle crosses the line from the center of the ridge to the origin at roughly 90° as shown in the sketch in Fig. 5b in Sec. III.B. Both angles $\alpha = 13.6°$ and $\beta = 14.2°$ are considerably close, and therefore the orientation of the convective ridge is approximately perpendicular to the line from its center to the origin of the plot. Note that the deviation between α and β is of the order of magnitude of the standard error predicted by the Monte Carlo simulation (approximately 1°) in Appendix B.

The spectrum at the lower frequency of 769 Hz, however, exhibits some different features: while the inclination of the convective ridge at $\alpha = 12.6°$ is similar to the higher frequency case, the entire convective ridge appears to be shifted downward. A line drawn from the origin of the spectrum to the center of the convective ridge reveals an angle of $\beta = -5.1°$ and therefore is not aligned perpendicular to the ridge orientation.

3. *Comparison of Results*

Figure 8 shows the results of all three estimation methods plotted against frequency: $\hat{\alpha}$ determined by the spatial method [cf. Eq. (5)], α determined by the wavenumber inclination method [cf. Eq. (14)], and β determined by the wavenumber center method [cf. Eq. (12)].

For all three methods, strong outliers appear mainly at the harmonics of the electrical noise fundamental frequency (i.e., 800, 1200, 1600 Hz, etc.). Apart from those outliers, the results of the spatial method vary very slightly. The wavenumber domain method based on the inclination of the convective ridge shows good agreement with the spatial method in the frequency range above 800 Hz. Again, the deviation between those two methods is of the order of magnitude of the standard error (approximately 1°) predicted by the Monte Carlo simulation (Appendix B). However, the results of the wavenumber method based on the center of the convective ridge differ more

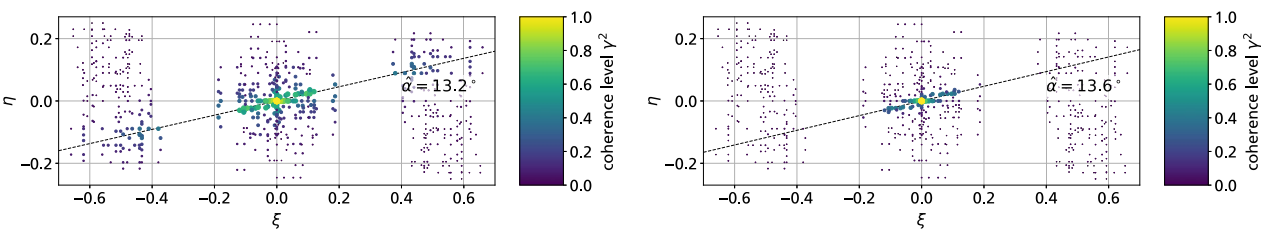

a) f = 769 Hz b) f = 2490 Hz

Fig. 6 Coherence patches from experimental data and angles determined from spatial coherence fit.

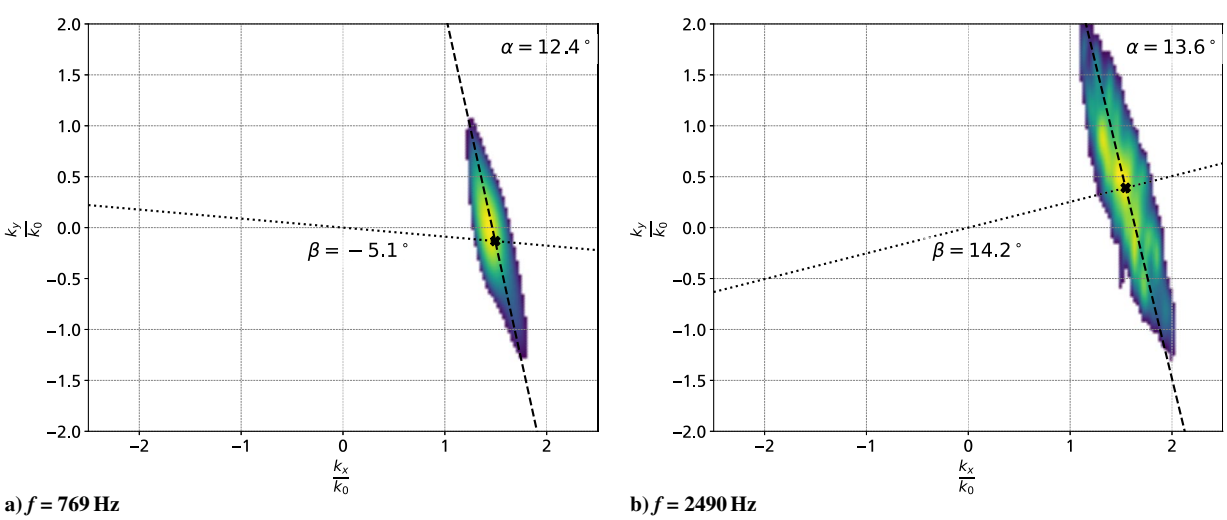

a) f = 769 Hz b) f = 2490 Hz

Fig. 7 Wavenumber spectrum from experimental data.

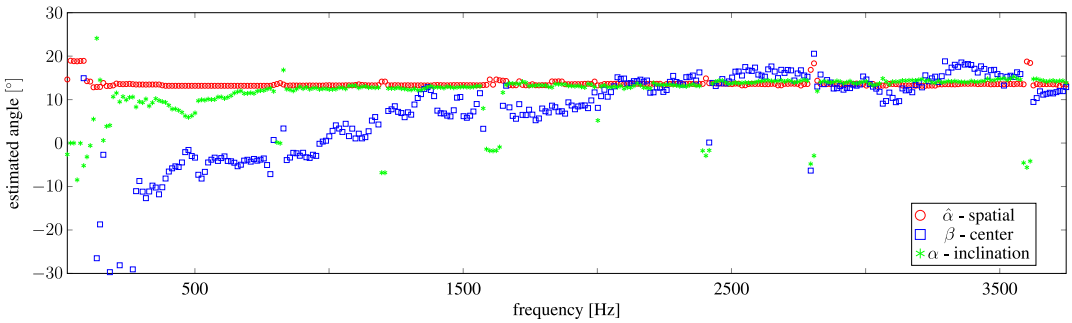

Fig. 8 Angle estimation results for all frequencies below 3750 Hz.

Downloaded by DLR DEUTSCHES ZENTRUM FUER LUFT UND RAUMFAHRT on December 13, 2022 | http://arc.aiaa.org | DOI: 10.2514/1.J061711

significantly from the other two methods. For frequencies above 2000 Hz, the results of method the center approach are in the same range as those of the other two methods, but the variations are much larger. Moreover, for frequencies below 2000 Hz the estimated angle according to the center approach deviates strongly from the other two methods. This effect increases with decreasing frequency.

The observed phenomenon of a displacement of the convective ridge in the wavenumber domain will be discussed in more detail in the following Sec. IV.B.

B. Tilted Coherent Structures Leading to Shifted Convective Ridges

Considering the observations so far, the question arises which properties of the flow cause a deviation of the signals' convective phase properties from the coherence properties. In the following, a comprehensive model will be derived that accounts for the observed phenomena. A simple model of a coherent turbulent structure interacting with a simple two-transducer array is shown in Fig. 9.

The simplified array consists of just two transducers n_1 and n_2, which are separated by distance ξ' in flow direction and by distance η' in crossflow direction, respectively. The turbulent structure is represented by a straight line inclined at an angle β relative to the array y axis and moves according to the convective velocity u_c. The orientation of the flow direction with the array is represented by angle α. Hence, the inclination of the coherent turbulent structure relative to the crossflow direction is $\beta - \alpha$. It is assumed that the turbulent structure locally imprints a similar pressure footprint onto the transducers, once they are directly underneath the turbulent structure. This implies that the dispersion of pressure is only due to convection and not due to other effects that may propagate ahead of the structure or sideways. Using this simple model, the time difference Δt between the pressure signals at transducers n_1 and n_2 can be derived as a function of transducer separations ξ' and η' and the angle of inclination of the turbulent structure, $\beta - \alpha$. It is

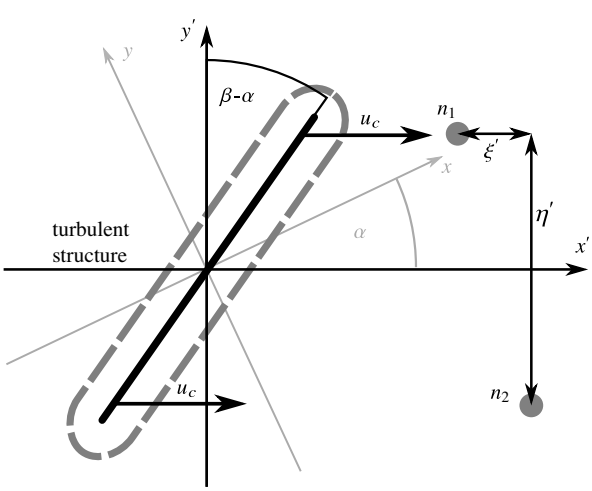

Fig. 9 Model of a tilted coherent turbulent structure passing over a two-transducer array. Here, u_c is inclined by angle α relative to the array coordinates x and y to yield the flow coordinate system x' and y'.

$$\Delta t(\xi', \eta', \alpha, \beta, u_c) = \frac{1}{u_c}(\xi' + \eta' \tan(\beta - \alpha)) \tag{15}$$

which reduces to the regular model with $\Delta t = \xi'/u_c$ for $\beta = \alpha$. Using the relationship $\Delta t = \Delta x/u_c$ with $\Delta x = \theta\lambda/2\pi$ and λ being the wavelength of pressure fluctuations, the time difference Δt between the two transducers can be depicted as a phase shift θ in the spatial domain

$$\theta(\xi', \eta', \alpha, \beta, \lambda) = \frac{2\pi}{\lambda} \cdot (\xi' + \eta' \tan(\beta - \alpha)) \tag{16}$$

The wavelength λ is a function of frequency: $\lambda = u_c/f$; thus

$$\theta(\xi', \eta', \alpha, \beta, f, u_c) = \frac{2\pi f}{u_c} \cdot (\xi' + \eta' \tan(\beta - \alpha)) \tag{17}$$

A synthetic cross-spectral matrix is set up and evaluated to demonstrate the effects of the introduced model. As each entry of a cross-spectral matrix represents a transducer combination separated by ξ and η, Eq. (17) can be used to determine the phase shift for each entry at a given frequency f. For the transducer positions that lead to the transducer separations ξ and η, the same positions as were used in the flight test are applied (cf. Sec. II). The setup of the cross-spectral matrix is given by

$$R(\xi', \eta', l_x, l_y, \alpha, \beta, f) = \gamma(l_x, l_y, \alpha) \cdot \varphi(\theta(\xi', \eta', \alpha, \beta, f, u_c)) \tag{18}$$

In Eq. (18), α is again the tilt of the coherence patch in the spatial domain resulting from the coherence levels γ between the signals of different transducer pairs:

$$\gamma(l_x, l_y, \alpha) = \exp\left(-\frac{|\xi'(\alpha)|}{l_x} - \frac{|\eta'(\alpha)|}{l_y}\right) \tag{19}$$

The rotated separation coordinates ξ' and η' are defined by

$$\begin{aligned} \xi'(\alpha) &= \cos(\alpha)\xi + \sin(\alpha)\eta \\ \eta'(\alpha) &= -\sin(\alpha)\xi + \cos(\alpha)\eta \end{aligned} \tag{20}$$

The phase propagation $\varphi(\theta)$ is set by using θ from Eq. (17):

$$\varphi(\theta) = \exp(i \cdot \theta) \tag{21}$$

For simplicity, the amplitude of R is set to 1 for all frequencies. For coherence length and convective velocity magnitude values of similar magnitude as the ones expected from the flight test were used to set up the synthetic data. The evaluation was performed using the beamforming approach in Eq. (7), and the resulting dirty maps were postprocessed using DAMAS2.1 [23] to remove influence of the point-spread function. The resulting wavenumber spectra from the synthetically produced cross-spectral matrices for the frequency $f = 769$ Hz are shown in Fig. 10. The case shown in Fig. 10a represents an event where the flow is aligned with the x axis and no inclination of the turbulent structures occurs. The convective ridge is centered on

Downloaded by DLR DEUTSCHES ZENTRUM FUER LUFT UND RAUMFAHRT on December 13, 2022 | http://arc.aiaa.org | DOI: 10.2514/1.J061711

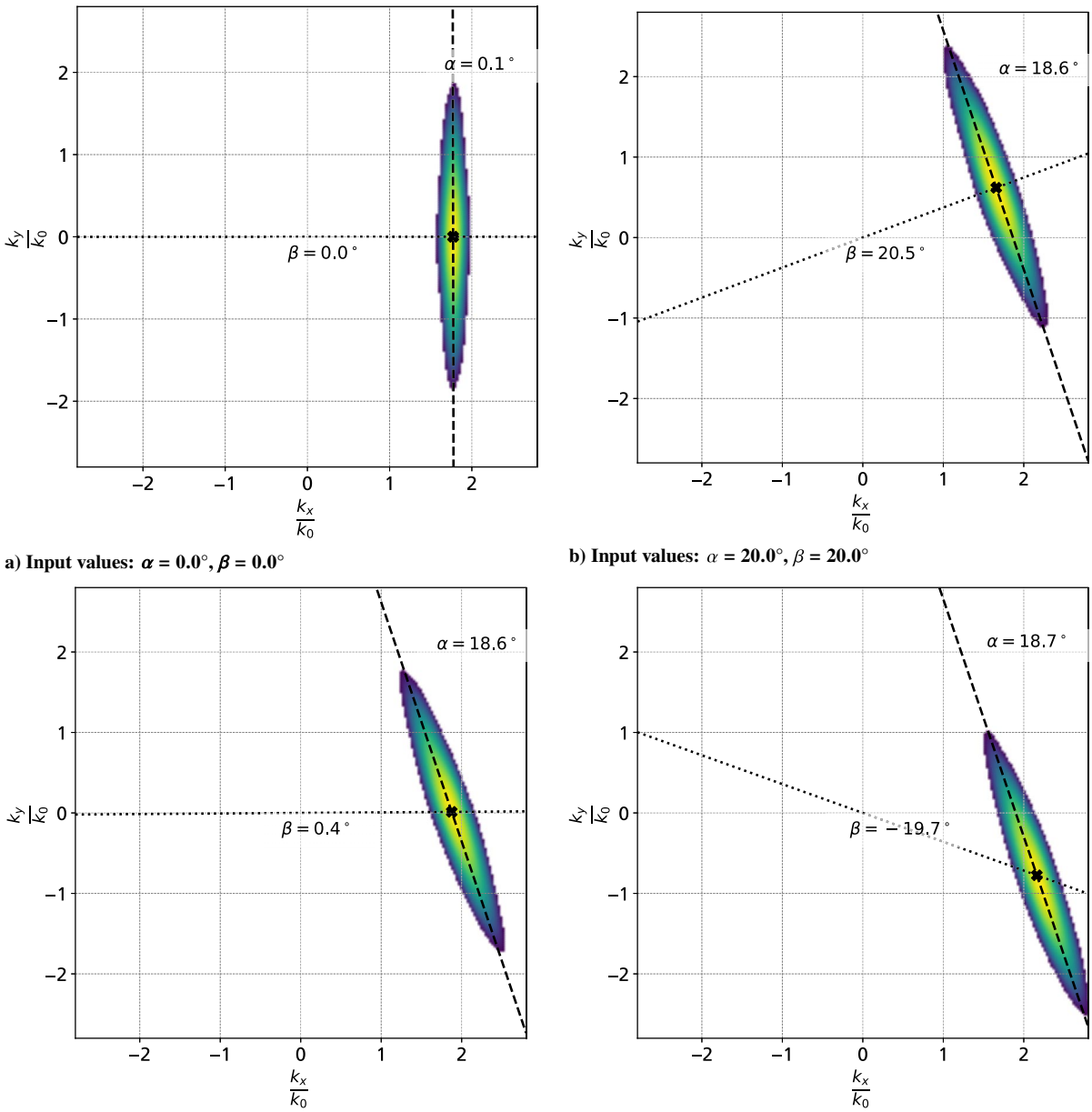

a) Input values: α = 0.0°, β = 0.0°

b) Input values: α = 20.0°, β = 20.0°

c) Input values: α = 20.0°, β = 0.0°

d) Input values: α = 20.0°, β = −20.0°

Fig. 10 Wavenumber spectrum from processed synthetic data (f = 769 Hz).

the x axis, and its orientation is perpendicular to the x axis. The modeled cross-spectral matrix was set up with both α and β set to 0.0°. The output of the data analysis returns $\alpha = 0.1°$ and $\beta = 0.0°$.

When the input values are set to $\alpha = 20.0°$ and $\beta = 20.0°$, the entire convective ridge is rotated about the origin of the wavenumber spectrum. This can easily be conceived as the previous case, but rotating the entire transducer array underneath the turbulent boundary layer by an angle of 20.0°. The turbulent structures are not tilted relative to the flow direction. Processing the dataset returns values of $\alpha = 18.6°$ and $\beta = 20.5°$.

When α and β are chosen to differ, e.g., $\alpha = 20.0°$ and $\beta = 0.0°$, a result as shown in Fig. 10c occurs. The convective ridge is still inclined at α, but its center is now located at $k_y/k_0 = 0$, which results from β. The analysis after processing returns $\alpha = 18.6°$ and $\beta = 0.4°$.

Taking this further and choosing $\alpha = 20.0°$ and $\beta = -20.0°$ results in the wavenumber spectrum shown Fig. 10d. Again, the convective ridge is tilted by α, but its center is now located at $k_y/k0 < 0$ at an angle of β relative to the origin of the spectrum. Analyzing this dataset returns $\alpha = 18.7°$ and $\beta = -19.7°$.

All the values of α and β that were used to set up the modeled cross-spectral matrix data were retrieved back from the data by analysis within an error range of 1.5°. This demonstrates that a tilted propagation of turbulent structures in the boundary layer causes a shift of the convective ridge in the wavenumber spectrum. Note that this requires that the tilt angle of the turbulent structures that pass over the array do have a nonzero mean. Otherwise, this effect would not be visible after the averaging procedure during Welch's method.

C. Extending the Exponential Wavenumber Spectrum Model

To insert the phase angle into the existing models for wavenumber representation of turbulent boundary-layer pressure fluctuations, a modification is proposed in the following. The modified model for wavenumber spectrum Φ will utilize separate angles for the coherence pattern and the phase propagation. The model is retrieved by separately applying a Fourier transform to the coherence patch and to the propagation term.

$$\Phi(k_x, k_y, \alpha, \beta, f) = \frac{1}{(2\pi)^2} \int_{-\infty}^{\infty} \int_{-\infty}^{\infty} \gamma(\xi, \eta, \alpha, f) \cdot \varphi(\xi, \eta, \alpha, \beta, f) \cdot \exp(-i(k_x\xi + k_y\eta))\, \mathrm{d}\xi\, \mathrm{d}\eta \tag{22}$$

Downloaded by DLR DEUTSCHES ZENTRUM FUER LUFT UND RAUMFAHRT on December 13, 2022 | http://arc.aiaa.org | DOI: 10.2514/1.J061711

Here, $\gamma(\xi, \eta, \alpha, f)$ is the coherence pattern used by Corcos [18] and Efimtsov [16], which is expanded by the angle α [cf. Eq. (19)]. The propagation proposed by the same authors is modeled using $\varphi(\xi, \eta, \alpha, \beta, f)$, which has been expanded by the angles α and β:

$$\varphi(\xi, \eta, \alpha, \beta, f) \tag{23}$$

The integral in Eq. (22) solves to

$$\begin{aligned}\Phi(k_x, k_y, \alpha, \beta, f) &= \frac{l_x(f) l_y(f)}{\pi^2} \cdot \frac{1}{1 + l_x^2(f)(k_x \cos(\alpha) + k_y \sin(\alpha) - k_c)^2} \\ &\cdot \frac{1}{1 + l_y^2(f)(-k_x \sin(\alpha) + k_y \cos(\alpha) - k_c \tan(\beta - \alpha))^2}\end{aligned} \tag{24}$$

and can be scaled by an amplitude $A(f)$. Here k_c is the convective wavenumber (based on the convective velocity), which can be obtained via the convective velocity u_c from models like Smol'yakov [17]:

$$k_c(f) = \frac{2\pi f}{u_c} \tag{25}$$

A detailed derivation of Eq. (24) can be found in Appendix A.

V. Discussion

Tilted turbulent structures may affect the determination of propagation velocity. The next section discusses how this affects the analysis of wavenumber spectra. Additionally, a short discussion on the predominant direction of tilting in the present case will be discussed as well as the cases in which the tilted propagation may affect surface excitation prediction. For most parts of the section we assume for simplicity that the array is aligned with the flow direction, i.e., $\alpha = 0°$.

A. Effects on Determination of Propagation Velocity

A shift in the convective ridge can have an effect on the propagation velocity determined from the position of the convective ridge. As summarized by, for instance, Bull [12], the center of the convective ridge is associated with the convective velocity $u_c = 2\pi f / \|k^{\text{center}}\|_2$. Bull only describes the one-dimensional case with $k_y = 0$. In the two-dimensional case, the wavenumber spectrum is extended in crossflow direction (as used throughout the present investigation). Similar to the one-dimensional case, the convective velocity is determined from the displacement of the center of the convective from the origin $u_c = 2\pi f / \|k^{\text{center}}\|_2$. This applies as well for a mere change in flow direction, which can be viewed as a simple rotation of the array underneath a constant flow. The question arises whether or not this still holds for tilted propagation of turbulent structures. It will be discussed in the following using Figs. 11a–11c and 12a–12c.

In a simple example in Fig. 11a, a nontilted structure is sketched to pass in x direction over a linear array. When analyzed in the wavenumber domain, sketched in Fig. 11c, this will lead to a convective ridge centered at position $\|k^{\text{center}}\|_2 = 2\pi f / u_c$ with $u_c = a/\Delta t$. Due to the single dimension of the array, the resulting wavenumber spectrum will be one-dimensional as well because no information is available on the characteristic of the turbulent structure in y direction. If the coherent structure is tilted by β as shown in Fig. 11b, the linear array will gather the same information as in the case with the nontilted structure. The position of the convective ridge in the wavenumber spectrum will therefore not change.

Using a two-dimensional array as shown in Fig. 12a yields additional information in y direction and allows for the wavenumber spectrum to extend in k_y direction. A nontilted turbulent structure passing over such an array would lead to a two-dimensional convective ridge. A slice through this two-dimensional wavenumber spectrum at $k_y = 0$ rad/m would yield the convective ridge at a similar position $\|k^{\text{center}}\|_2$ as in the one-dimensional case.

A tilted structure passing over the array causes the convective ridge to be shifted downward by an angle β as shown in Fig. 12c. Its amplitude at the intersection point with the k_x axis is lowered relative to its center. However, the position of the intersection with the k_x axis remains unchanged compared to the nontilted case, as each one-dimensional line in the array will still produce the same result as in the

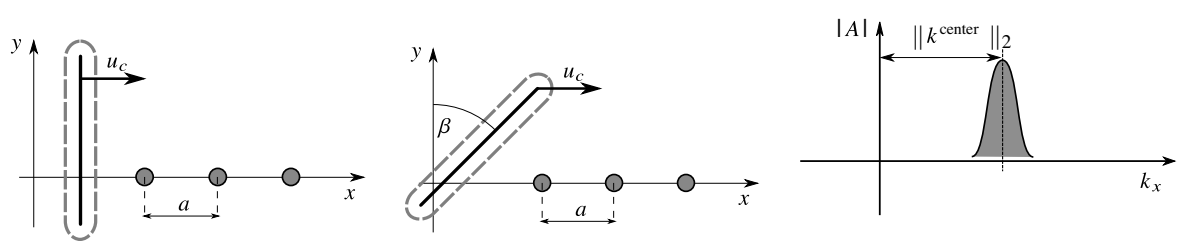

a) Regular turbulent structure passing over a one-dimensional array

b) Tilted turbulent structure passing over a one-dimensional array

c) One-dimensional wavenumber spectrum and the position of the convective ridge at convective wavenumber

Fig. 11 Scenarios with turbulent structures and a one-dimensional array.

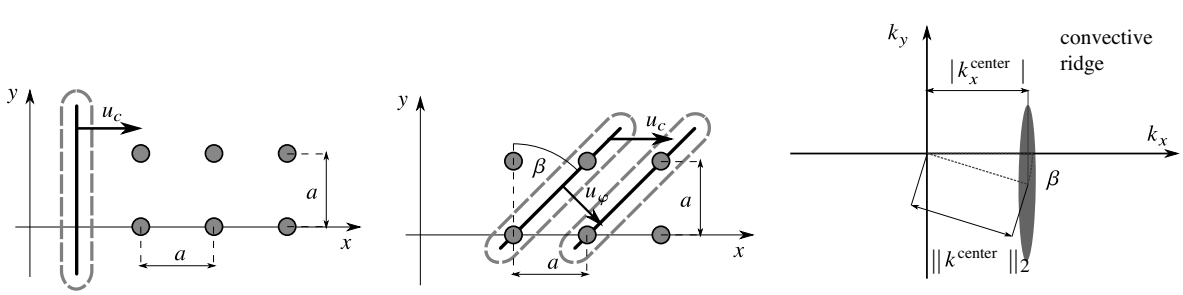

a) Regular turbulent structure passing over a two-dimensional array

b) Tilted turbulent structure passing over a two-dimensional array

c) Wavenumber spectrum with a shifted convective ridge and two possible values for the convective wavenumber

Fig. 12 Scenarios with turbulent structures and a two-dimensional array.

Downloaded by DLR DEUTSCHES ZENTRUM FUER LUFT UND RAUMFAHRT on December 13, 2022 | http://arc.aiaa.org | DOI: 10.2514/1.J061711

solely one-dimensional case. The intersection of the convective ridge with the k_x axis therefore represents the value of $|k_x^{\text{center}}|$. The downward shift of the center of the convective ridge results in an increased value of $\|k^{\text{center}}\|_2$ compared to $|k_x^{\text{center}}|$, which represents a lower propagation velocity.

In Fig. 12b, the passing of the inclined structure over the array is sketched. In the time period Δt it takes the structure to cover the distance a, the array "observes" the structure to pass in the direction of u_φ at an angle β. To the array, the distance apparently covered in the time Δt appears to be only $\tilde{a} = a\cos(\beta)$. Therefore, the apparent convective velocity is reduced to $u_\varphi = \tilde{a}/\Delta t = u_c \cos(\beta)$. In the wavenumber domain, the center of the convective ridge is shifted away from the origin with increasing β by $k_\varphi = 2\pi f/u_\varphi = 2\pi f/(u_c \cos(\beta))$.

This virtual decrease in propagation velocity has to be considered when modeling wavenumber spectra with tilted convective ridges for the use in structural vibration excitation. When modeling the position of the convective ridge, a convective velocity model such as the one from Smol'yakov [17] is consulted. The design of the experiment used by Smol'yakov was most likely tailored to determining the convective velocity u_c and no tilt of the turbulent structures will have occurred. (In the case of Smol'yakov, the data were taken from a water tunnel experiment with known flow direction and a flow-aligned array). When these data are used to model wavenumber spectra with tilted convective ridges, their position will be erroneously close to the origin of the spectrum, as the shift of the convective ridge comes with a virtual decrease of u_c to u_φ.

On the other hand, when a wavenumber spectrum is used to derive information about the propagation velocity of turbulent structures in the boundary layer, it has to be considered that the position of the convective ridge only resembles the "virtual" propagation velocity and not the physical passing of turbulent structures over the array.

B. Predominant Orientation of Tilted Turbulent Structures

In the present case the shifting of the convective ridge is observed downward in the wavenumber spectrum, toward smaller values of k_y (as sketched in Fig. 12c). The orientation of the convective ridge remains constant. When looking at Figs. 13 and 14 it can be seen that the phase response between the two transducers will be opposite when the sign of β changes.

A downward shift toward smaller values of k_y present in the current experimental data (cf. Figs. 7a and 7b) indicates that the turbulent structures are tilted as shown in Fig. 14: the upper part of the structures appears to precede the lower part.

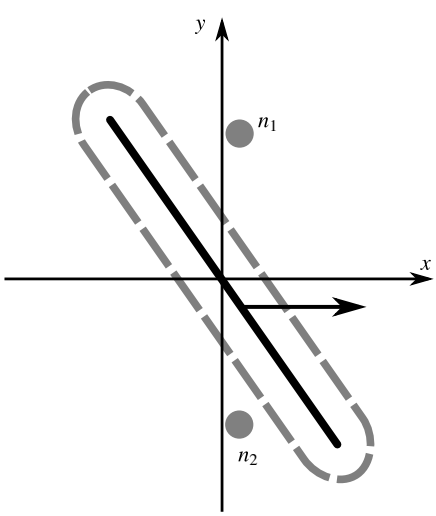

Fig. 13 Tilted turbulent structure with $\beta < 0$. The coherent signal will arrive at transducer n_2 before transducer n_1, thus implying propagation in positive y direction.

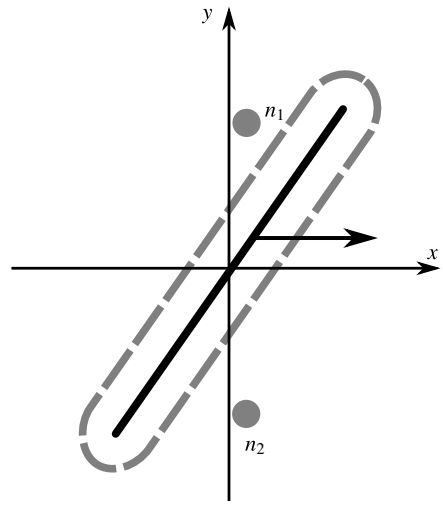

Fig. 14 Tilted turbulent structure with $\beta > 0$. The coherent signal will arrive at transducer n_1 before transducer n_2, thus implying propagation in negative y direction.

C. Summary of Formulas

For the general case of an array that is not necessarily aligned with the flow (i.e., $\alpha \neq 0$), the proportions discussed in the last section generalize to

$$u_\varphi = u_c \cos(\beta - \alpha) \tag{26}$$

$$k_\varphi \cos(\beta - \alpha) = k_c \tag{27}$$

Moreover, substituting $k_c = k_\varphi \cos(\beta - \alpha)$ in Eq. (24) we get the equivalent representation of the wavenumber spectrum model in terms of k_φ:

$$\begin{aligned}\Phi(k_x, k_y, \alpha, \beta, f) &= \frac{l_x(f) l_y(f)}{\pi^2} \cdot \frac{1}{1 + l_x^2(f)(k_x \cos(\alpha) + k_y \sin(\alpha) - k_\varphi \cos(\beta - \alpha))^2} \\ &\quad \cdot \frac{1}{1 + l_y^2(f)(-k_x \sin(\alpha) + k_y \cos(\alpha) - k_\varphi \sin(\beta - \alpha))^2}\end{aligned} \tag{28}$$

D. Past Considerations in Vibroacoustic Prediction

The prediction of cabin noise through structural vibration has been used in the frequency range from 500 Hz and 5 kHz by Graham [19]. In his prediction method the flow is assumed to be aligned with the length axis of the structure. Graham states that the key to a good prediction is to have an accurate description of the convective peak in case of hydrodynamic coincidence at high aircraft speeds. The accurate description in his terms is the knowledge about its position as well as its shape. While the shape of the convective ridge is more important at higher frequencies, its position becomes more important at lower frequencies. The long coherence lengths of the turbulent structures in the flow at lower frequencies lead to a sharper but higher peak of the convective ridge. When a sharp convective ridge occurs, its position relative to the dominant modes becomes important. It is due to this characteristic that both the rotation and the shift of the convective ridge at low frequencies are important to consider in prediction.

VI. Conclusions

Flight test data were analyzed to obtain both spatial coherence patterns and wavenumber spectra of surface pressure fluctuations. These two representations of fluctuations were analyzed for characteristic features connected to the flow direction deviating from the array orientation. Mainly, these features can be described for both the

Downloaded by DLR DEUTSCHES ZENTRUM FUER LUFT UND RAUMFAHRT on December 13, 2022 | http://arc.aiaa.org | DOI: 10.2514/1.J061711

spatial coherence pattern and the wavenumber spectra as a rotation about the origin. However, in some cases observed in the present investigation, the wavenumber domain representation of the pressure fluctuations deviated from the solely rotational behavior about the origin and an additional shift of the convective ridge was observed. A tilted convection of turbulent structures was discussed as a possible cause for the observed behavior and incorporated in an analytical model for the wavenumber representation of the data. Due to the specific measurement setup, a meaningful calibration of the pressure sensors could not be carried out. This leads to uncertainties regarding the amplitudes of the CSM entries. However, an erroneous level of amplitudes in the CSM does mainly affect the magnitude of the frequency-wavenumber spectrum. For the present analysis, only the center and orientation of the convective ridge were used. These features are not expected to be strongly affected by a variation in the magnitude of the amplitudes in the CSM.

In a subsequent discussion, a dominant tilt direction of the turbulent structures in the flow was specified. Besides the insight into the events within the turbulent boundary layer, the importance of the topic lies in the prediction of fuselage structural vibration. The phase characteristic of convection and therefore the position of the convective ridge in the wavenumber domain are crucial for the excitation characteristic of the boundary-layer pressure fluctuations.

We want to emphasize here that this paper primarily wants to present the phenomenon of shifted convective ridges that was observed in the flight test dataset. Tilted convection is suggested by the authors as a possible cause of this phenomenon along with a suitable analytical model. However, we do not claim that this is actually the reason for the observed shift of the convective ridge in this measurement but only state this as a conjecture. Moreover, the possible mechanisms that may cause such a tilted convection are not discussed here as this is far beyond the scope of this work.

Appendix A: Fourier Transform of the Tilted Coherence Pattern

The Fourier transform of the tilted coherence pattern with the shifted propagation angle will be derived in the following. Starting point is the functions $\gamma(\xi, \eta, \alpha, f)$ (representing the coherence decay) and $\varphi(\xi, \eta, \beta, f)$ (representing the propagation), as introduced in Sec. IV.B:

$$\gamma(\xi,\eta,\alpha,f) = \exp\left(-\frac{|\xi\cos(\alpha)+\eta\sin(\alpha)|}{l_x(f)} - \frac{|-\xi\sin(\alpha)+\eta\cos(\alpha)|}{l_y(f)}\right) \tag{A1}$$

$$\varphi(\xi,\eta,\beta,f) = \exp(i\cdot k_c(\xi\cos(\alpha)+\eta\sin(\alpha) + \tan(\beta-\alpha)(-\xi\sin(\alpha)+\eta\cos(\alpha)))) \tag{A2}$$

Here ξ and η are the transducer separations in x and y direction, respectively; α is the tilt angle of the coherence pattern (and thus similarly the inclination angle of the convective ridge); and β is the angle from the origin of the wavenumber spectrum to the center of the convective ridge. Taking the spatial Fourier transform of $\gamma\cdot\varphi$ yields

$$\Phi(k_x,k_y,\alpha,\beta,f) = \frac{1}{(2\pi)^2}\int_{-\infty}^{\infty}\int_{-\infty}^{\infty}\gamma(\xi,\eta,\alpha,f)\cdot\varphi(\xi,\eta,\beta,f) \cdot\exp(-i(k_x\xi+k_y\eta))\,\mathrm{d}\xi\,\mathrm{d}\eta \tag{A3}$$

Equation (A3) is written in terms of the aircraft coordinate system. It is related to the coordinate system of the tilted coherence pattern (denoted by u, v) via

$$\begin{pmatrix}\cos(\alpha) & -\sin(\alpha)\\ \sin(\alpha) & \cos(\alpha)\end{pmatrix}\begin{pmatrix}u\\ v\end{pmatrix} = \begin{pmatrix}\xi\\ \eta\end{pmatrix} \tag{A4}$$

The Jacobian determinant of the transformation in Eq. (A4) is 1, so that

$$d\xi\,d\eta = \left|\det\frac{\partial(\xi,\eta)}{\partial(u,v)}\right| du\,dv = du\,dv \tag{A5}$$

The Fourier transform is then written as

$$\Phi(k_x,k_y,\alpha,\beta,f) = \frac{1}{(2\pi)^2}\int_{-\infty}^{\infty}\int_{-\infty}^{\infty}\exp\left(-\frac{|u|}{l_x(f)}-\frac{|v|}{l_y(f)}\right) \cdot\exp(-i(k_x(u\cos(\alpha)-v\sin(\alpha))+k_y(u\sin(\alpha)+v\cos(\alpha)))) \cdot\exp(ik_c(u+v\tan(\beta-\alpha)))\,\mathrm{d}u\,\mathrm{d}v \tag{A6}$$

This can be split into separate integrals:

$$\Phi(k_x,k_y,\alpha,\beta,f) = \frac{1}{(2\pi)^2}\int_{-\infty}^{\infty}\exp\left(-\frac{|u|}{l_x(f)}-iu(k_x\cos(\alpha)+k_y\sin(\alpha)-k_c)\right)\mathrm{d}u \cdot\int_{-\infty}^{\infty}\exp\left(-\frac{|v|}{l_y(f)}-iv(-k_x\sin(\alpha)+k_y\cos(\alpha)-k_c\tan(\beta-\alpha))\right)\mathrm{d}v \tag{A7}$$

which can be reduced to

$$\Phi(k_x,k_y,\alpha,\beta,f) = \frac{1}{(2\pi)^2}\int_{-\infty}^{\infty}\exp\left(-\frac{|u|}{l_x(f)}-iup\right)\mathrm{d}u \cdot\int_{-\infty}^{\infty}\exp\left(-\frac{|v|}{l_y(f)}-ivq\right)\mathrm{d}v \tag{A8}$$

by using

$$p = k_x\cos(\alpha)+k_y\sin(\alpha)-k_c \tag{A9}$$

and

$$q = -k_x\sin(\alpha)+k_y\cos(\alpha)-k_c\tan(\beta-\alpha) \tag{A10}$$

This can be evaluated by splitting up the ranges of integration:

$$\begin{aligned}\Phi(k_x,k_y,\alpha,\beta,f) = \frac{1}{4\pi^2}\cdot&\int_0^{\infty}\exp\left(-u\left(\frac{1}{l_x(f)}+ip\right)\right)\mathrm{d}u\\ &+\int_{-\infty}^{0}\exp\left(u\left(\frac{1}{l_x(f)}-ip\right)\right)\mathrm{d}u\\ \cdot&\int_0^{\infty}\exp\left(-v\left(\frac{1}{l_y(f)}+iq\right)\right)\mathrm{d}v\\ &+\int_{-\infty}^{0}\exp\left(v\left(\frac{1}{l_y(f)}-iq\right)\right)\mathrm{d}v\end{aligned} \tag{A11}$$

This yields the Fourier transform

$$\Phi(k_x,k_y,\alpha,\beta,f) = \frac{4l_x(f)l_y(f)}{4\pi^2(1+l_x^2(f)p^2)(1+l_y^2(f)q^2)} \tag{A12}$$

Substituting for p and q again yields

$$\Phi(k_x,k_y,\alpha,\beta,f) = \frac{l_x(f)l_y(f)}{\pi^2}\cdot\frac{1}{1+l_x^2(f)(k_x\cos(\alpha)+k_y\sin(\alpha)-k_c)^2} \cdot\frac{1}{1+l_y^2(f)(-k_x\sin(\alpha)+k_y\cos(\alpha)-k_c\tan(\beta-\alpha))^2} \tag{A13}$$

Note that α and β may be dependent on frequency as well, so that $\alpha = \alpha(f)$ and $\beta = \beta(f)$.

Downloaded by DLR DEUTSCHES ZENTRUM FUER LUFT UND RAUMFAHRT on December 13, 2022 | http://arc.aiaa.org | DOI: 10.2514/1.J061711

Appendix B: Error Estimation

To estimate the error in determining the flow angle for each of the three presented methods, a Monte Carlo simulation was performed by simulating noisy cross-spectral data with a noise variance corresponding to the variance in the measured cross-spectral matrix R:

$$\hat{\sigma}_{nm}^2 := \mathrm{Var}(R_{nm}) \tag{B1}$$

The values $\hat{\sigma}_{nm}^2$ were estimated by sample variances on the set of block samples during the computation of Welch's method. We refer to [26] for a deeper investigation of this statistical quantity. The noise-free synthetic CSM entries are given by

$$R_{nm}^{\mathrm{exact}} = A(f) \cdot \exp\left(i\xi'_{nm}\frac{2\pi f}{u_c}\right) \cdot \exp\left(-\frac{|\xi'_{nm}|}{l_x} - \frac{|\eta'_{nm}|}{l_y}\right) \tag{B2}$$

To perform the simulation on a physically meaningful parameter setup, the following considerations were made:

Table B1 Parameter settings for the Monte Carlo simulation

Parameter	Value
Angle, $\hat{\alpha}$	13°
Convective velocity, u_c	168 m/s
Frequencies, f	$f = 500$–3500 Hz; increments of 500 Hz
Coherence length, l_x	$l_x = \frac{u_c}{0.1 \cdot 2\pi f}$ m
Coherence length, l_y	$l_y = \frac{u_c}{2\pi f}$ m
Amplitudes, A	From flight test data
Number of Monte Carlo samples, $n_{\max}$	500
CSM variances, $\hat{\sigma}_{mn}^2$	From flight test data [cf. Eq. (B1)]

1) The amplitude value $A(f)$ was estimated by the CSM of the flight test data by

$$A(f) = \frac{1}{N}\sum_{n=1}^{N} R_{nn}(f)$$

2) $u_c = 0.8 \cdot 210$ m/s, where 210 m/s is in the range of the freestream velocity during the flight test, and the factor 0.8 is motivated by the empirical investigations in [17].

3) $l_x = u_c/0.1 \cdot 2\pi f$ and $l_y = u_c/2\pi f$, where the factor 0.1 and the ratio l_y/l_x are chosen in the range of the empirical investigations in [16,27].

The entire set of selected parameters is summarized in Table B1.

The uncertainty can now be estimated by a simulation approach for a sufficiently large sample of cross spectrum. This is possible, because we know the empirical variances of the experimental cross-spectrum estimates [cf. Eq. (B1)]. The generic procedure given in Algorithm 1 works for any method $\mathcal{F}$ that maps an (empirical) cross-spectral matrix R to an estimation of the angle $\hat{\alpha}$. The results of the Monte Carlo simulation are summarized in Table B1. We observe that all three methods provide reasonably good angle estimations with a standard error that is strictly less than 2.5°. However, the spatial method is by far the most accurate one with a standard error in the order of 0.1°. This low level of variation of the results was also observed in the evaluation of the experimental dataset. Both wavenumber domain methods have a standard error in the order of 1°. For most frequencies, the method based on the inclination of the convective ridge performs better than the one based on the center estimation. Only at 1500 Hz the inclination method has a significantly larger error than the center method.

Concerning the two wavenumber domain methods, it seems that the center approach is a bit more robust against noise effects in the DAMAS 2.1 result, while the inclination approach provides a more accurate angle estimate in most cases. Note further that the wavenumber domain methods depend on the specific setup of the DAMAS

Algorithm 1: Generic method for uncertainty estimation

input : $\mathcal{F}$ angle estimation method, $n_{\max}$, $\hat{\sigma}_{mn}^2$, $\hat{\alpha}$, l_x, l_y, f, u_c, A
output $\mathrm{err}_{\mathrm{std}}$ approximation of standard deviation of the angle estimation error
:
initialize $R^{\mathrm{exact}} = R^{\mathrm{exact}}(A, f, u_c, l_x, l_y, \hat{\alpha})$ `// exact CSM cf. Eq. (B2)`
$\mathrm{err}_{\mathrm{std}} := 0$
for $n = 1, \ldots, n_{\max}$ **do**
  sample X, Y from $[\mathcal{N}(0,1)]^{N\times N}$ `// real Gaussian white noise matrices`
  define $Z \in \mathbb{C}^{N\times N}$ by `// Hermitian noise matrix with correct scaling`
  $Z_{nm} := \sqrt{\frac{\hat{\sigma}_{nm}^2}{2}} \cdot (X_{nm} + X_{mn} + iY_{nm} - iY_{mn})$
  $R^{\mathrm{noisy}} := R^{\mathrm{exact}} + Z$ `// noisy CSM`
  $\alpha^{\mathrm{est}} := \mathcal{F}(R^{\mathrm{noisy}})$ `// angle estimation`
  $\mathrm{err}_{\mathrm{std}} = \mathrm{err}_{\mathrm{std}} + \frac{1}{n_{\max}}|\alpha^{\mathrm{est}} - \hat{\alpha}|^2$ `// sample average of squared error`
end
$\mathrm{err}_{\mathrm{std}} = \sqrt{\mathrm{err}_{\mathrm{std}}}$

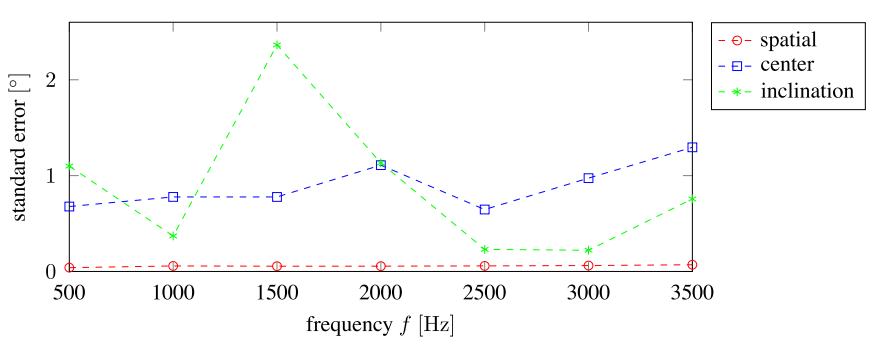

Fig. B1 Estimated standard error from the Monte Carlo simulation for all three considered methods.

2.1 method, especially the number of iterations. For the results presented here the number of iterations was set to 1000. Hence, increasing the number of DAMAS 2.1 iterations may also help to improve the accuracy of the wavenumber domain methods.

Acknowledgments

This research has received funding through two different projects: 1) MEMS microphone usage in aeroacoustic applications: project *ADEC (LPA)* from the Clean Sky 2 Joint Undertaking (JU) under grant agreement No. 945583, and 2) the "Flight-LAB/OVAL" research project within the aerospace research program (LuFo V2; Support code 20 K1511C) supported by the Federal Ministry for Economic Affairs and Energy. The authors wish to acknowledge the Federal Ministry for Economic Affairs and Energy (BMWi) for the financial support of the flight test as part of the "SIMKAB" research alliance within the aerospace research program (LuFo IV; Support code 20 K0805G) and for the financial support of the "COCLEA/NEMO" research project within the aerospace research program (LuFo IV; Support code 20 K1102F); Airbus S.A.S. for the provided infrastructure and help on modifications of the flight test carrier; and the DLR Institute of Aero-Elasticity, DLR Institute of Flight Systems, and the DLR Flight Experiment team for the help provided in the preparation and performance of the flight test.

References

[1] Haxter, S., and Spehr, C., "Comparison of Model Predictions for Coherence Length to In-Flight Measurements at Cruise Conditions," *Journal of Sound and Vibration*, Vol. 390, March 2017, pp. 86–117. https://doi.org/10.1016/j.jsv.2016.10.038

[2] Arguillat, B., Ricot, D., Robert, G., and Bailly, C., "Measurements of the Wavenumber-Frequency Spectrum of Wall Pressure Fluctuationis Under Turbulent Flows," *11th AIAA/CEAS Aeroacoustics Conference*, AIAA Paper 2005-2855, May 2005. https://doi.org/10.2514/6.2005-2855

[3] Manoha, E., "The Wavenumber-Frequency Spectrum of the Wall Pressure Fluctuations Beneath a Turbulent Boundary Layer," *AIAA and CEAS Aeroacoustics Conference*, AIAA Paper 1996-1758, 1996. https://doi.org/10.2514/6.1996-1758

[4] Prigent, S. L., Salze, E., Jondeau, E., and Bailly, C., "Spatial Structure and Wavenumber Filtering of Wall Pressure Fluctuations on a Full-Scale Cockpit Model," *Experiments in Fluids*, Vol. 61, No. 9, 2020, pp. 1–14. https://doi.org/10.1007/s00348-020-03017-2

[5] Hu, Z. W., Morfey, C. L., and Sandham, N. D., "Aeroacoustics of Wall-Bounded Turbulent Flows," *AIAA Journal*, Vol. 40, No. 3, 2002, pp. 465–473. https://doi.org/10.2514/2.1697

[6] Gyorgyfalvy, D., "Effect of Pressurization on Airplane Fuselage Drag," *Journal of Aircraft*, Vol. 2, No. 6, 1965, pp. 531–537. https://doi.org/10.2514/3.43693

[7] Panton, R. L., Lowery, R. L., and Reischman, M. M., "A Theoretical and Flight Test Study of Pressure Fluctuations under a Turbulent Boundary Layer. Part 2: Flight Test Study," NASA-CR-140448, 1967, https://ntrs.nasa.gov/api/citations/19740025684/downloads/19740025684.pdf.

[8] Rizzi, S. A., Rackl, R. G., and Andrianov, E. V., "Flight Test Measurements from the Tu-144LL Structure/Cabin Noise Follow-On Experiment," 2000, https://ntrs.nasa.gov/api/citations/20000038213/downloads/20000038213.pdf.

[9] Palumbo, D., "Determining Correlation and Coherence Lengths in Turbulent Boundary Layer Flight Data," *Journal of Sound and Vibration*, Vol. 331, No. 16, 2012, pp. 3721–3737. https://doi.org/10.1016/j.jsv.2012.03.015

[10] Abraham, B. M., and Keith, W. L., "Direct Measurements of Turbulent Boundary Layer Wall Pressure Wavenumber-Frequency Spectra," *Journal of Fluids Engineering*, Vol. 120, No. 1, 1998, pp. 29–39. https://doi.org/10.1115/1.2819657

[11] Haxter, S., Spehr, C., Hartmann, M., Ocker, J., Tokuno, H., and Wickern, G., "Improving the Performance of Aeroacoustic Measurements Beneath a Turbulent Boundary Layer in a Wake Flow," *AIAA Aviation*, AIAA Paper 2014-3289, 2014. https://doi.org/10.2514/6.2014-3289

[12] Bull, M. K., "Wall-Pressure Fluctuations Beneath Turbulent Boundary Layers: Some Reflections on Forty Years of Research," *Journal of Sound and Vibration*, Vol. 190, No. 3, Feb. 1996, pp. 299–315. https://doi.org/10.1006/jsvi.1996.0066

[13] Panda, J., Roozeboom, N. H., and Ross, J. C., "Wavenumber-Frequency Spectra on a Launch Vehicle Model Measured via Unsteady Pressure-Sensitive Paint," *AIAA Journal*, Vol. 57, No. 5, May 2019, pp. 1–17. https://doi.org/10.2514/1.J057449

[14] Willmarth, W. W., and Wooldridge, C. E., "Measurements of the Fluctuating Pressure at the Wall Beneath a Thick Turbulent Boundary Layer," *Journal of Fluid Mechanics*, Vol. 14, Oct. 1962, pp. 187–210. https://doi.org/10.1017/S0022112062001160

[15] Palumbo, D., "The Variance of Convection Velocity in the Turbulent Boundary Layer and its Effect on Coherence Length," *Journal of Sound and Vibration*, Vol. 332, No. 15, July 2013, pp. 3692–3705. https://doi.org/10.1016/j.jsv.2013.02.010

[16] Efimtsov, M. M., "Characteristics of the Field of Turbulent Pressures at the Wall of a Boundary Layer," *Soviet Physics Acoustics*, Vol. 28, No. 4, 1982, p. 4.

[17] Smol'yakov, A. V., "A New Model for the Cross Spectrum and Wavenumber-Frequency Spectrum of Turbulent Pressure Fluctuations in a Boundary Layer," *Acoustical Physics*, Vol. 52, No. 3, 2006, pp. 331–337. https://doi.org/10.1134/S1063771006030146

[18] Corcos, G. M., "Resolution of Pressure in Turbulence," *Journal of the Acoustical Society of America*, Vol. 35, No. 2, 1963, pp. 192–199. https://doi.org/10.1121/1.1918431

[19] Graham, W. R., "A Comparison of Models for the Wavenumber-Frequency Spectrum of Turbulent Boundary Layer Pressures," *Journal of Sound and Vibration*, Vol. 206, No. 4, 1997, pp. 541–565. https://doi.org/10.1006/jsvi.1997.1114

[20] Spehr, C., Hennings, H., Buchholz, H., Bouhaj, M., Haxter, S., and Hebler, A., "In-Flight Sound Measurements: A First Overview," *18th AIAA/CEAS Aeroacoustics Conference*, AIAA Paper 2012-2208, June 2012. https://doi.org/10.2514/6.2012-2208

[21] Welch, P. D., "The Use of Fast Fourier Transform for the Estimation of Power Spectra: A Method Based on Time Averaging over Short, Modified Periodograms," *IEEE Transactions on Audio and Electroacoustics*, Vol. 15, No. 2, 1967, pp. 70–73. https://doi.org/10.1109/TAU.1967.1161901

[22] Ehrenfried, K., and Koop, L., "Experimental Study of Pressure Fluctuations Beneath a Compressible Turbulent Boundary Layer," *14th AIAA/CEAS Aeroacoustics Conference*, AIAA Paper 2008-2800, 2008. https://doi.org/10.2514/6.2008-2800

[23] Haxter, S., "Extended Version: Improving the DAMAS 2 Results for Wavenumber-Space Beamforming," *Proceedings on CD of the 6th Berlin Beamforming Conference*, Paper BeBeC-2016-D8, GFaI, Gesellschaft zu Förderung angewandter Informatik e.V., Berlin, Feb. 2016, http://www.bebec.eu/Downloads/BeBeC2016/Papers/BeBeC-2016-D8.pdf.

[24] Chase, D. M., "Modeling the Wavevector-Frequency Spectrum of Turbulent Boundary Layer Wall Pressure," *Journal of Sound and Vibration*, Vol. 70, No. 1, 1980, pp. 29–67. https://doi.org/10.1016/0022-460X(80)90553-2

[25] Jayamaran, S., Esakkirajan, S., and Veerakumar, T., *Digital Image Processing*, Tata McGraw–Hill Education, New Delhi, 2009, pp. 152–242.

[26] Raumer, H.-G., Spehr, C., Hohage, T., and Ernst, D., "Weighted Data Spaces for Correlation-Based Array Imaging in Experimental Aeroacoustics," *Journal of Sound and Vibration*, Vol. 494, March 2021, Paper 115878. https://doi.org/10.1016/j.jsv.2020.115878

[27] Farabee, T. M., and Casarella, M. J., "Spectral Features of Wall Pressure Fluctuations Beneath Turbulent Boundary Layers," *Physics of Fluids A: Fluid Dynamics*, Vol. 3, No. 10, 1991, pp. 2410–2420. https://doi.org/10.1063/1.858179

L. Ukeiley
Associate Editor

Downloaded by DLR DEUTSCHES ZENTRUM FUER LUFT UND RAUMFAHRT on December 13, 2022 | http://arc.aiaa.org | DOI: 10.2514/1.J061711